

Microfluidic Mixing for Biosensors

N. Scott Lynn Jr.

Abstract Among other factors, the performance of an affinity-based biosensor is dependent on the rate at which analyte is transported to, and captured by, its active sensing surface. The efficiency of analyte delivery can be increased via the use of microfluidics, albeit not without detraction, as microfluidic biosensors are often subjected to severe diffusion limitations when used for the detection of biologically relevant analytes. Such conditions lead to the formation of a boundary layer, void of analyte, which acts to resist the rate at which analyte is captured. It is often proposed to mix the fluid in the sensing chamber, where the exchange of depleted solution with fresh analyte can potentially increase sensor performance. The nature of analyte transport in a mixed channel is complex, however, and simply mixing the contents of a microchannel does not guarantee success. In this chapter, we review developments in the characterization (and prediction of) analyte transport in both mixed and unmixed channels. Our discussion focuses on the conditions under which mixing will (and will not) be beneficial and furthermore, the magnitude of performance increase that can be expected. Special attention is given to flow in the staggered herringbone mixer (SHM): a passive chaotic micromixer often used to enhance the performance of a biosensor. We review relevant experimental works on the topic and compare the results from several studies with the behavior expected from theory. Finally, we note several challenging aspects regarding the detection of circulating tumor cells which, due to their large size, are subject to additional transport mechanisms with respect to smaller analytes.

Keywords Biosensor • Microfluidics • Mixing • Chaos
Transport phenomena • Circulating tumor cell

N.S. Lynn Jr. (✉)
Institute of Photonics and Electronics, Academy of Sciences of the
Czech Republic, Chaberská 57, 18251 Prague, Czech Republic
e-mail: lynn@ufe.cz

© Springer International Publishing AG 2018
S.-H. Oh et al. (eds.), *Miniature Fluidic Devices for Rapid Biological Detection*,
Integrated Analytical Systems, https://doi.org/10.1007/978-3-319-64747-0_3

1 Introduction

Affinity-based biosensors represent an increasingly prevalent analytic tool for detection, research, and (bio)analytic purposes. Reports on such devices span a period of nearly three decades—their use has become omnipresent across both research and commercial settings—where end-use applications include medical diagnostics and drug discovery, as well as agricultural, environmental, and food monitoring [1].

The scope of these devices is extremely broad: transduction mechanisms can proceed via optical [2–4], electrochemical [5, 6], micromechanical [7], piezoelectric [8], thermometric [9], and magnetic means [10]. In addition, the list of biorecognition elements is just as large and includes antibodies, enzymes, and engineered proteins; nucleic acids and aptamers; and tissues, cells, and microorganisms. The bulk of these devices are surface-based, whereby the biorecognition elements are immobilized to a region on, or near, the active transduction element(s).

For most of these devices, the sensor output (i.e., the sensor signal) is proportional to the rate of analyte captured by the active regions of the sensor surface. In general, this condition remains independent of both the transduction mechanism and the nature of the biorecognition element. To increase the efficiency of analyte delivery, biosensing devices are often paired with a microfluidic flow cell: a trend that grew rapidly after the advent of low-cost, user-friendly, and time-efficient microfabrication methods [11, 12]. The inherently small dimensions of a microchannel allow for reduced sample volume requirements (ranging from mL down to μL) and perhaps more importantly, enhanced sensor response times [13].

The majority of microfluidic biosensors are constructed in a fairly simple manner, whereby a rectangular microchannel is situated over a planar sensing surface having immobilized biorecognition elements.¹ A schematic of this generalized layout is shown in Fig. 1, and Table 1 lists the pertinent geometrical and operational parameters. The majority of biosensing processes are operated with pressure-driven flow, as optimal conditions for electrokinetic flows (e.g., DC or AC electroosmosis [14]) are not often compatible for surface-based biosensors. Due to the small characteristic lengths, pressure-driven microchannel flows are associated with a low Reynolds number, $\text{Re} = \rho UH/\mu < 100$, where flows are uniaxial and void of turbulence.

Under certain (and often encountered) conditions, microfluidic biosensors can exhibit inconvenient behavior. Biosensors having a relatively large sensing region size with fast interaction kinetics are often diffusion-limited, where the resulting analyte depletion layer acts to resist analyte delivery. In such cases, an increase in sensor response can be obtained with a higher sample flow rate (i.e., higher rate of analyte delivery), albeit at the sacrifice of efficient sample use: a 10 \times increase in sensor response frequently necessitates a 1000 \times increase in flow rate [15]. Benefits can also be obtained by simple changes to the flow cell geometry, for example, by decreasing the channel height [16]; however, such changes are limited by large

¹The area for signal transduction is often the same as that for biocomponent immobilization, which is assumed herein.

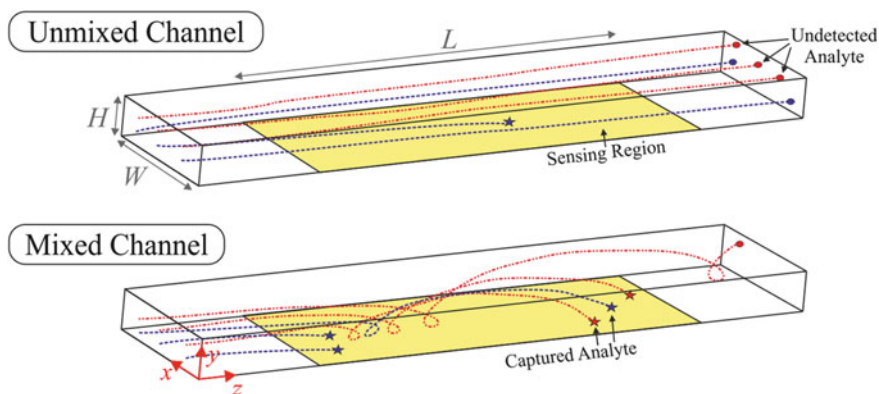


Fig. 1 The uniaxial flow in microfluidic channels often leads to a large percentage of analyte that does not interact with the sensing surface. The inclusion of mixing can increase the efficiency of analyte capture

Table 1 List of the dimensional parameters and values for the experimental sensors used in this study

| Dimensional Parameter | Symbol | Units |
|---------------------------------------------|------------|---------------------------------------------|
| <i>Geometrical Parameters</i> | | |
| Microchannel height | H | mm |
| Microchannel width | W | mm |
| Length of sensing region | L | mm |
| <i>Operational Parameters</i> | | |
| Volumetric flow rate | Q | $\text{mm}^3 \text{s}^{-1}$ |
| Fluid viscosity | μ | $\text{g mm}^{-1} \text{s}^{-1}$ |
| Fluid density | ρ | g mm^{-3} |
| Diffusivity of analyte | D | $\text{mm}^2 \text{s}^{-1}$ |
| <i>Kinetic Parameters</i> | | |
| Association rate constant | k_1 | $\text{mm}^3 \text{mol}^{-1} \text{s}^{-1}$ |
| Dissociation rate constant | k_2 | s^{-1} |
| Average surface density of bioreceptors | Γ_o | mol mm^{-2} |
| <i>Dependent Parameters</i> | | |
| Average surface density of captured analyte | Γ | mol mm^{-2} |
| Analyte collection flux | J | $\text{mol mm}^{-2} \text{s}^{-1}$ |

increases in viscous resistance. Methods to remove the analyte boundary layer, either by fluid sheathing [17] or by fluidic removal of the depleted fluid [18], come at the cost of increased complexity.

The problems associated with diffusion-limited biosensors originate from the uniaxial flow profile inherent to rectangular microchannels at low Re . This problem can be alleviated by mixing the fluid above the sensing region. The exchange of depletion layers with fresh solution can potentially increase both the rate of analyte capture

and the efficiency of sample use. The use of mixing to enhance mass (or heat) transfer in laminar flows is a long-studied problem within both chemical and mechanical engineering disciplines [19, 20].

Microfluidic mixing, however, is a relatively complex process, and extensive lengths often need to be taken to ensure proper mixing conditions. The literature on microfluidic mixing is quite extensive and, in general, can be separated into two broad categories. The first category encompasses *active* mixers, which utilize an external energy source to manipulate and mix fluid, typically in a controllable manner. Active mixers operate through a variety of mechanisms, among which include electroosmotic, electrophoretic, magnetic, and electrothermal effects. The second category encompasses *passive* mixers, which rely on the geometry of the microchannel to mix fluid and thus require no additional power, albeit often in a noncontrollable manner. Passive mixing strategies are generally based on either channel modifications to introduce non-axial flow (e.g., mixing grooves), or channel arrangements such that the flow is systematically split and recombined. There are currently a number of reviews dedicated to both groups of micromixers, to which we refer the reader [21–25].

Upon scanning the literature, one finds that only a small percentage of the literature on microfluidic mixing is dedicated to improving biosensor performance. The vast majority of these studies are focused on the staggered herringbone mixer (SHM), a passive mixer that mixes fluid in a chaotic fashion [26]. Of these studies, there are a wide range of reported values regarding level of improvement that can be attributed to the inclusion of mixing. For example, the performance improvement via the use of the SHM have ranged from 0% [27] to 26% [28] for the detection of streptavidin, whereas a similar mixer offered a 170% improvement for the detection of circulating tumor cells (CTCs) [29].

Therefore, before beginning an attempt to modify an existing biosensor with the inclusion of a microfluidic mixer (taken individually, both processes are quite complicated), it is important to ask the following two questions:

- (A) Is an improvement in sensing performance expected?
- (B) If so, what is the expected magnitude of improvement?

This chapter aims to provide the answers to both of these questions. We start by reviewing the concepts related to the mass transfer of analyte in an unmixed microchannel, specifically, the convective and diffusive transport of analyte and its (reactive) capture. We use these concepts to estimate the conditions under which a biosensor can be expected to be diffusion- or reaction-limited.² We then review, from a theoretical perspective, how the inclusion of mixing might serve to increase rates of analyte transport and furthermore, how to predict such rates. Finally, we review the literature on the use of the staggered herringbone mixer for biosensing purposes and compare the results from several experimental studies with the behavior expected from theory.

²As discussed later, the distinction between the two is very important: a reaction-limited biosensor will never benefit from the inclusion of mixing.

Before starting, however, it is worth noting that this topic also maintains relevance within a variety of other fields. In addition to (bio)sensing applications, control over the mass transfer of a dissolved species to the wall of a microchannel is sought after in a variety of other applications, including microfluidic fuel cells [18], the controlled deposition of nanostructured materials [30], continuous flow (heterogeneous) catalytic microreactors [31], and membrane absorbers [32].

2 Analyte Transport in Unmixed Channels

The capture of analyte by a microfluidic biosensor maintains a complex dependency on a number of factors, including the architecture of both the microchannel and sensing regions, the flow rate of sample solution, the diffusivity of analyte, and several (kinetic) parameters related to the interaction between biorecognition element and analyte. Fortunately, both convection and diffusion are well-understood phenomena on the microfluidic scale, where fluid is restricted to the laminar regime ($Re < 100$).

A number of theoretical, computational, and experimental reports have analyzed the problem related to unmixed sensors. Particularly useful to this chapter are those by Myszka et al. [33] and Squires et al. [15]. In this section, we summarize the problem related to unmixed sensors and furthermore, provide a simple guide to predict analyte transport to a generalized biosensor as shown in Fig. 1.

2.1 Governing Equations

The capture of an analyte in a microchannel is best described in mathematical terms. For steady, laminar, incompressible flow, the velocity vector field $\mathbf{v} = \mathbf{v}(x, y, z)$ is represented by both the Stokes equation

$$-\nabla p + \mu \nabla^2 \mathbf{v} = 0 \quad (1)$$

and the equation of continuity,

$$\nabla \cdot \mathbf{v} = 0. \quad (2)$$

where $p = p(x, y, z)$ is the fluid pressure, and a no-slip condition $\mathbf{v} = 0$ is assumed on the channel walls. For pressure-driven flows in rectangular channels (low Re , sufficiently far from the inlet), the x - and y -components of the fluid velocity vanish (i.e., the flow becomes uniaxial), and the solution to both Eqs. (1) and (2) can be solved via a Fourier series solution as

$$v_z = \frac{2U \left[1 - \left(\frac{2y}{H} \right)^2 + 4 \sum_{n=0}^{\infty} \frac{(-1)^{n+1}}{m_n^3 \cosh\left(\frac{m_n W}{H}\right)} \cosh\left(\frac{2m_n x}{H}\right) \cos\left(\frac{2m_n y}{H}\right) \right]}{\frac{4}{3} - \frac{8H}{W} \sum_{n=0}^{\infty} m_n^{-5} \tanh\left(\frac{m_n W}{H}\right)}, \quad (3)$$

where $m_n = \pi(2n + 1)/2$, and the domain consists of the region $-W/2 < x < W/2$ and $-H/2 < y < H/2$. Often microchannels are fabricated with dimensions such that $W \gg H$, whereby edge effects can be ignored and the fluid velocity profile becomes only a function of y , where the velocity profile then follows

$$v_z = \frac{3U}{2} \left(1 - 4 \frac{y^2}{H^2} \right). \quad (4)$$

The concentration of analyte in the microchannel $c = c(x, y, z, t)$ is described by the unsteady convection–diffusion equation,

$$\frac{\partial c}{\partial t} + \mathbf{v} \cdot \nabla c = D \nabla^2 c. \quad (5)$$

To account for the capture of analyte a standard ligand–receptor mechanism is often assumed, $A_s + B \rightleftharpoons AB$, where A_s represents the aqueous analyte present at the sensor surface (with concentration $c_s = c_s(x, z, t)$), B represents the immobilized (free) receptor (with surface density $\beta = \beta(x, z, t)$), and AB the bound analyte/receptor complex (with surface density $\gamma = \gamma(x, z, t)$).

Under proper conditions the analyte will interact only with the sensing region (where receptors are immobilized), whereby the remaining surfaces will resist the adsorption of analyte and can be considered to be passivated. Assuming elementary reaction kinetics and ignoring surface diffusion, the boundary conditions for Eq. (5) along each respective surface can thus be written as

$$\text{sensing region: } \hat{n} \cdot D \nabla c = k_1 c_s \beta - k_2 \gamma, \quad (6)$$

$$\text{passivated surfaces: } \hat{n} \cdot D \nabla c = 0, \quad (7)$$

where \hat{n} is the normal unit vector along the sensing region. Equation (6) represents the balance between the transport of aqueous analyte toward the sensor surface (or more specifically, its diffusive flux $D \nabla c$) with the rate of analyte capture on said surface. The rate of analyte capture can be written in terms of an analyte collection flux $j = j(x, z, t)$, where

$$j = \frac{\partial \gamma}{\partial t} = k_1 c_s \beta - k_2 \gamma. \quad (8)$$

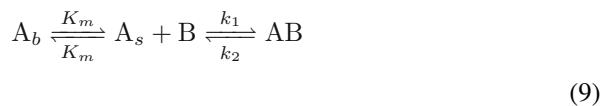
This value is especially pertinent to biosensing, as the response of a biosensor is often proportional to γ (the density of captured analyte), rather than the absolute number of captured analyte molecules.

Unfortunately, Eq. (8) cannot be used directly to calculate this flux, as the distribution of c_s is unknown without the solution to Eqs. (5)–(7). An analytical solution to these equations is not possible due to the parabolic nature of the pressure-driven velocity profile. Approximate solutions can be obtained by assuming a linear velocity profile, yet they are only valid for “fast” flows having small boundary layers. Discrete solutions can be obtained via computational methods (typically via finite-element or finite-volume methods); however, even modern computational packages can be quite cumbersome and furthermore, the problem has an extensive parameter space (seen in Table 1).

2.2 Macroscopic Approach: Averaged Rates of Transport

Rather than examination of analyte transport in a microscopic manner (i.e., the solutions of Eqs. (5)–(7) over the entire sensing chamber), it is useful to examine the problem from a macroscopic point of view. In this approach, one assumes that the sensor response can be sufficiently estimated via knowledge of $\Gamma = \Gamma(t)$: the *average* surface density of captured analyte over the sensing region.

Given the (experimentally measurable) parameters shown in Table 1, estimations of Γ , or more appropriately $d\Gamma/dt$, can be obtained in a relatively simple manner by assuming the process of analyte capture occurs in two steps: (i) the convective and diffusive transport of analyte from the bulk solution to the sensor surface and (ii) the affinity-based capture of said analyte by immobilized bioreceptors. A reaction mechanism for such a process can be written as



where A_b represents aqueous analyte far from the sensing region (with concentration C_o). The rate constants for the first step in Eq. (9) are represented by the macroscopic mass transfer coefficient K_m , defined as

$$J = K_m(C_o - C_s), \quad (10)$$

where $C_s = C_s(t)$ is the average analyte concentration along the sensor surface, and $J = J(t)$ is the average analyte capture flux over the sensor surface.³ As shown later, K_m is related to the shape and size of the analyte boundary layer, and is dependent on many of the parameters listed in Table 1.

³The rate at which the first step in Eq. (9) proceeds is dependent only on the magnitude of the difference between C_s and C_o , and hence the presence of K_m in both the forward and reverse steps.

The reaction mechanism in Eq. (9) can be used to formulate a set of two coupled ordinary differential equations, obtained via a mass balance over A_s and AB, respectively:

$$\frac{dC_s}{dt} = K_m C_o - K_m C_s - k_1 C_s (\Gamma_o - \Gamma) + k_2 \Gamma, \quad (11)$$

$$\frac{d\Gamma}{dt} = k_1 C_s (\Gamma_o - \Gamma) - k_2 \Gamma, \quad (12)$$

where Γ_o is the average surface density of immobilized bioreceptors.

We first examine the behavior of these two equations in the limits where mass transport occurs both very fast and very slow with respect to the rate of reactive capture. The former can be taken as the case where $K_m \rightarrow \infty$, whereby the solution to Eq. (11) leads to $C_s \rightarrow C_o$. This represents the reaction-limited regime (sometimes referred to as being “well-mixed”), where Eq. (11) can be used to estimate the rate of analyte collection as $d\Gamma/dt = k_1 C_o (\Gamma_o - \Gamma) - k_2 \Gamma$.

The opposite situation represents the diffusion-limited regime, where mass transfer is slow and $K_m \rightarrow 0$; in the initial stages of such an assay, the amount of captured analyte is small ($\Gamma \approx 0$) and it follows that $C_s \rightarrow 0$. These conditions lead to the formation of an analyte boundary layer with variable shape and size (see Fig. 2). When such boundary layer has reached a steady state, the rate of analyte collection can be estimated as $d\Gamma/dt = K_m C_o$.

Equations (11) and (12) can be simplified by noting that the capture of analyte will often have a relatively small impact on the shape and size of the analyte boundary layer.⁴ Under such conditions a quasi-steady approximation can be assumed, where $dC_s/dt \approx 0$, and Eq. (11) can be solved explicitly for C_s . Substitution into Eq. (12) then leads to

$$\frac{d\Gamma}{dt} = \frac{k_1 C_o (\Gamma_o - \Gamma) - k_2 \Gamma}{1 + k_1 (\Gamma_o - \Gamma) / K_m}. \quad (13)$$

The conditions under which a biosensor can be considered to be quasi-steady have been discussed by a variety of authors; more information can be found in the works by Squires et al. [15], Eddowes [34], and Glaser [35].

As seen in the denominator of Eq. (13), the relative magnitude of K_m with respect to $k_1 (\Gamma_o - \Gamma)$ aids to provide information on the limiting step in the reaction mechanism described by Eq. (9). The ratio of these two values is a dimensionless number known as the Damköhler number Da , defined here as $Da = k_1 \Gamma_o / K_m$, as we are often interested in the behavior of a sensor at the beginning of an assay. It follows that conditions leading to $Da \gg 1$ and $Da \ll 1$ represent a sensor that is diffusion- and reaction-limited, respectively.

This macroscopic approach is often referred to as a two-compartmental model and, as evidenced by its wide use in the biosensing community, can be quite useful; for conditions such that $Da \lesssim 1$, Eq. (13) is often used to extract bioanalytical

⁴More specifically, the characteristic time for the analyte boundary layer to reach equilibrium is often much smaller than the characteristic time for the analyte to reach equilibrium.

data (usually k_1 and k_2) from time-series biosensor signals [33, 36]. In addition, and especially pertinent to this chapter, Eq. (13) can be used to predict how changes in K_m will affect the sensor response.

We now have enough information to answer the first question: (A) is an improvement in sensing performance expected with the inclusion of mixing? In general—although, as seen later, not always true—analyte transport in mixed microchannels will be more efficient with respect to unmixed channels of similar dimension, where the process of mixing serves to increase the magnitude of K_m . However, this increase might be redundant: if an unmixed biosensor is operated under conditions such that $Da \ll 1$, then the inclusion of mixing will have no effect on the analyte collection rate.

Conversely, the performance of diffusion-limited biosensors can be increased significantly under mixed conditions: for an unmixed sensor with $Da \gg 1$, an increase in the analyte collection rate will be directly proportional to the increase in K_m .

This leads us to reformulate our second question: (B) how does a mixing process affect K_m ? Before attempting to answer that question, however, we must know the magnitude of K_m for an unmixed channel. In the next two sections, we give a brief review on predicting such values. Due to the extensive parameter space of the problem, it is convenient to work in dimensionless units.

2.3 Dimensionless Behavior

Analyte transport to a biosensor surface is best characterized by the Sherwood number, the dimensionless analog to the mass transfer coefficient. From the macroscopic perspective discussed in Sect. 2.2, the average Sherwood number can be calculated as

$$SH = \frac{JH}{(C_o - C_s)D} = \frac{K_m H}{D}. \quad (14)$$

It should be noted that we used the microchannel height as the characteristic length (rather than L), which allows for the direct comparison of SH between mixers having different lengths. As with the mass transfer coefficient, SH is an indicator of analyte transport efficiency to the sensing surface.

There are two dimensionless parameters that are important for the characterization (and prediction) of analyte transport to a biosensor. The first is the Péclet number, $Pe = UH/D$, which represents the relative magnitude between the rate of convective versus diffusive analyte transport on the scale of the microchannel. The second is the sensor aspect ratio $\eta = L/H$. For (steady) diffusion-limited analyte transport, these two parameters have a large influence on the size (δ) and shape of the analyte boundary layer; the former influences the rate of transport, whereas the latter determines the characteristics of transport.

Following the discussion by Squires et al. [15], the effect of Pe and η on the shape and size of a diffusion-limited analyte boundary layer is conveniently illus-

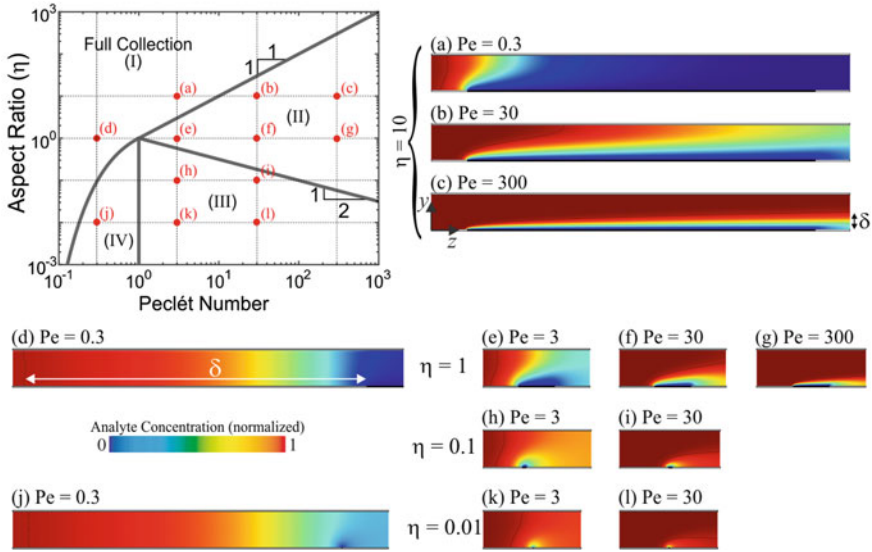


Fig. 2 Phase diagram for the steady, diffusion-limited analyte transport to a biosensor. The images shown in (a)–(l) are the steady analyte concentration profiles (across z and y) in a sufficiently wide microchannel, where the concentration of analyte along the sensing region was set to zero. These profiles were obtained using 2D finite-element simulations (COMSOL)

trated through the use of 2D finite-element simulations. Results from such simulations are shown in Fig. 2, where analyte transport in an unmixed channel can be classified into four “phases”, each of which regards a different boundary layer shape. The relative positions of the boundaries between each phase can be distinguished by both Pe and η , which can be used to define two additional dimensionless numbers.

The first of these is the Graetz number, $Gr = Pe/\eta$, which provides information on the development of the boundary layer in relation to the channel height. Conditions such that $Gr \lesssim 1$ (i.e., $Pe \lesssim \eta$) correspond to a completely developed analyte boundary layer,⁵ where the sensor will interact with all of the analyte flowing past. This relationship thus sets the boundary between phase (I) and (II); illustrations of this can be seen in the differences between (a), (b), and (c) in Fig. 2.

Another useful dimensionless parameter is the sensor Péclet number, $Pe_s = 6\eta^2Pe$, which represents the relative magnitude between convection versus diffusion adjusted for the size of the sensing region. For sufficiently fast flows (i.e., $Pe \gg 1$), diffusion-limited sensors with $Pe_s \gg 1$ will have boundary layers that are small with respect to both H and L , whereas sensors with $Pe_s \ll 1$ will have boundary layers that are small with respect to H , yet large with respect to L . This term can be used to classify the boundary between phase (II) and (III).

⁵Applicable for the geometries here, where a single wall acts to capture analyte. A value of $Gr \gg 1$ indicates the boundary layer has not reached the top of the channel.

Finally, the boundary between phase (III) and (IV) is determined by the value $Pe \approx 1$. The boundary between phase (I) and (IV) is slightly more complicated, and we refer the reader to previous works [15]. Nevertheless, we note that biosensors are rarely operated under conditions such that $Pe \leq 1$.

Before we discuss how the rate of analyte transport to a biosensor (i.e., SH, or K_m) can be predicted through knowledge of the relevant dimensionless parameters (i.e., Pe , η), we take a short pause to reconsider another form of question (A): is mixing worth the trouble? An qualitative answer to that question lies in the boundary layer profiles shown in Fig. 2. Intuition tells us that mixing will be most advantageous to sensors in phase (II); for example, there is a lot of “fresh” analyte just out of reach by the sensor in Fig. 2c. It is harder to deduce how mixing might affect sensors in phase (III); we leave this for later discussion (Sect. 3.1). Intuition also tells us that mixing will be of little use for sensors sufficiently far into phase (I): if $Pe \gg 1$ mixing might result in a local increase in analyte capture near the leading edge of the sensing region, yet it is clear that the averaged rate of analyte capture over the entire sensing region will remain unchanged; sensors operated at $Pe \lesssim 1$ are dominated by diffusion, and thus there will be no change in the rate of analyte collection by *any* portion of the sensor.⁶

2.4 Predicting Analyte Transport in Unmixed Sensors

Semi-quantitative estimates of the rate of diffusion-limited transport can be obtained through knowledge of the approximate boundary layer size: sensors in phase (I) have a boundary layer size of $\delta \approx H/Pe$ (measured along the channel axis), which according to Eq. (14),⁷ leads to a relatively accurate estimate of $SH \approx Pe/\eta$; sensors in phase (II) have a boundary layer size of $\delta \approx L \cdot Pe_s^{-1/3}$, which leads to an estimate of $SH \approx \eta^{-1}Pe_s^{1/3}$; and sensors in phase (III) have a boundary layer size that scales as $\delta \approx L \cdot Pe_s^{-1/2}$ (estimations of SH in this phase are more complicated).

Several authors have examined transport to unmixed sensors in a more quantitative fashion. Pertinent to this chapter are the works by Newman [37] and Ackerberg [38], who developed analytical solutions for SH as a function of Pe_s in the region of $Pe_s \gg 1$ and $Pe_s \ll 1$, respectively; these equations are listed in Table 2. Understandably, these equations are only valid under conditions relevant to phase (II) and (III). A slight correction of these equations in the respective limits of $Pe \approx \eta$ and $Pe \approx 1$ can be written as

$$SH^{-a} = (Pe/\eta)^{-a} + SH_o^{-a}, \quad (17)$$

⁶In this region, the rate of analyte capture is proportional to the flow rate, no matter how fast the fluid is stirred.

⁷Where the analyte flux in the axial direction can be estimated as $C_o D/\delta$, and thus $J \approx C_o DH/\delta L$.

Table 2 List of dimensionless parameters related to transport in unmixed channels and the equations used to calculate them. Equations (15) and (16) are taken from the works of Newman [37] and Ackerberg [38]. These equations are specific to sensors such as that shown in Fig. 1, where the channel is sufficiently wide ($W \gg H$) and the sensing region spans the entire width of the channel

| Dimensionless parameter | Equation |
|-------------------------|-------------------------------------------------------------------------------------------------------------------------------------------------------------------|
| Channel Péclet number | $Pe = Q/WD = UH/D$ |
| Sensor aspect ratio | $\eta = L/H$ |
| Sensor Péclet number | $Pe_s = 6\eta^2 Pe$ |
| Sherwood number: | |
| $Pe_s > 1$ | $SH_o = \frac{1}{\eta} \left(0.8075 Pe_s^{\frac{1}{3}} + 0.7058 Pe_s^{\frac{-1}{6}} - 0.1984 Pe_s^{\frac{-1}{3}} \right) \quad (15)$ |
| $Pe_s < 1$ | $SH_o = \frac{1}{\eta} \left[\pi G \left(1 - 0.04633 Pe_s G \right) \right], \quad (16)$ <p>where $G^{-1} = \ln(4 Pe_s^{\frac{-1}{2}}) + 1.0559$</p> |

where $a = 5/2$, and SH_o is taken from the results in Table 2. The term Pe/η represents the estimated Sherwood number in phase (I). Figure 3 illustrates the dependence of the Sherwood number on the Péclet number in unmixed sensors; it can be seen that Eq. (17) gives a very good match to data obtained from 2D FE simulations. Equations (15) and (16) have also been shown to match data from experiment [39]. In regards to the biosensing literature, the first term in Eq. (15) represents the mass transport coefficient used by the BIAevaluation software to extract kinetic data from SPR sensorgrams [36].

The use of the dimensionless numbers listed in Table 2 should not be deterring, as these parameters are often directly related to those commonly used in experiment. For example, the data shown in Fig. 3 represent how the rate of analyte capture by a biosensor (proportional to SH) is dependent on the flow rate (proportional to Pe) for sensors of varying length (proportional to η).

The use of the results in this section is thus fairly straightforward. The parameters directly affecting the mass transfer constant (U, H, L, D) are typically known beforehand and, if not, can be easily measured or estimated. These values can be used to calculate Pe, η , and Pe_s , which in turn can be used to calculate SH with the equations shown in Table 2. Equation (17) should be used when conditions are such that $Pe \approx \eta$ or $Pe \approx 1$; otherwise, the equations in Table 2 are fine when used alone. These values of SH can then be used directly with Eq. (14) to calculate the mass transfer coefficient K_m . This value, along with knowledge of both the kinetic parameters k_1 and k_2 as well as the density of bioreceptors Γ_o ,⁸ can be used to calculate the Damköhler number. If desired, these values can then be used with Eq. (13) to estimate the analyte collection rate as a function of time.

⁸Measurement of these values can be accomplished using a variety of methods, the most popular of which the SPR method.

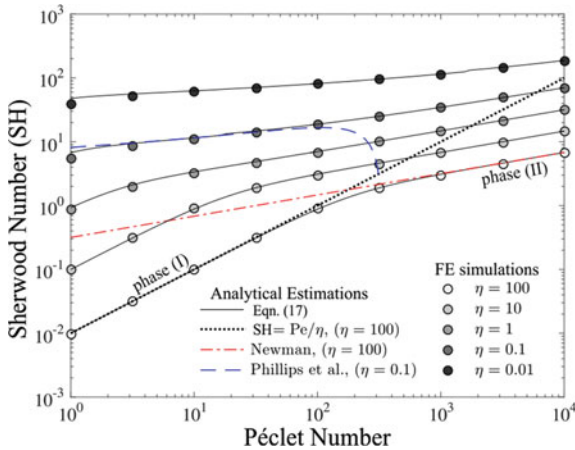


Fig. 3 The dependence of the Sherwood number on the Péclet number for biosensors having variable η . The black lines represent values of SH calculated from Eq. (17), where values of SH_0 were calculated from either Eqs. (15) or (16) (depending on the value of Pe_s). The black-dotted line pertains to estimates within phase (I) ($SH = Pe/\eta$). The red-dotted-dashed line represents the solution given by Newman [37] (Eq. (15)). The blue-dashed line represents the solution given by Akerberg [38] (Eq. (16)). The results shown as the symbols were obtained using 2D finite-element simulations (COMSOL), details of which are given in the work by Lynn and Homola [40]

3 Analyte Transport in Mixed Channels

In mixed channels, the velocity field is no longer uniaxial, as the effect of stirring induces a fluid movement transverse to the channel axis (i.e., in the x - and y -directions). Figure 4 illustrates how this additional fluid motion aids to stir the contents flowing through a “lid-driven” micromixer. Although this example is theoretical (a single moving wall on a microchannel presents several technical challenges), there are experimental devices that have similar flow profiles (e.g., an electroosmotically stirred microchannel [41]) and furthermore, this type of fluid motion has been shown to emulate the flow profile of the staggered herringbone mixer [42].

The fluid streamlines shown in Fig. 4 are indicative of analyte transport at very high Péclet numbers. From a biosensing perspective, this fluid motion would seemingly increase the rate of analyte capture. Yet, either of the two mixers shown in Fig. 4, used alone, would not provide optimal mixing conditions. Fluid streamlines in each device rotate around one or more stagnation points, thus only the analyte near the outer edges of each “vortex” will interact with a sensing region.

It is often a goal to design a micromixer (used for both mixing *and* biosensing purposes) such that fluid mixing proceeds in a chaotic fashion. The requirements to reach such a condition are fairly complex, and thus we point the reader to several useful sources [43–45]. In general, a chaotic mixing state can be achieved by periodic alteration of the flow profile along the channel axis, where alternating flow profiles do not have overlapping stagnation points. In doing so, the fluid is systematically

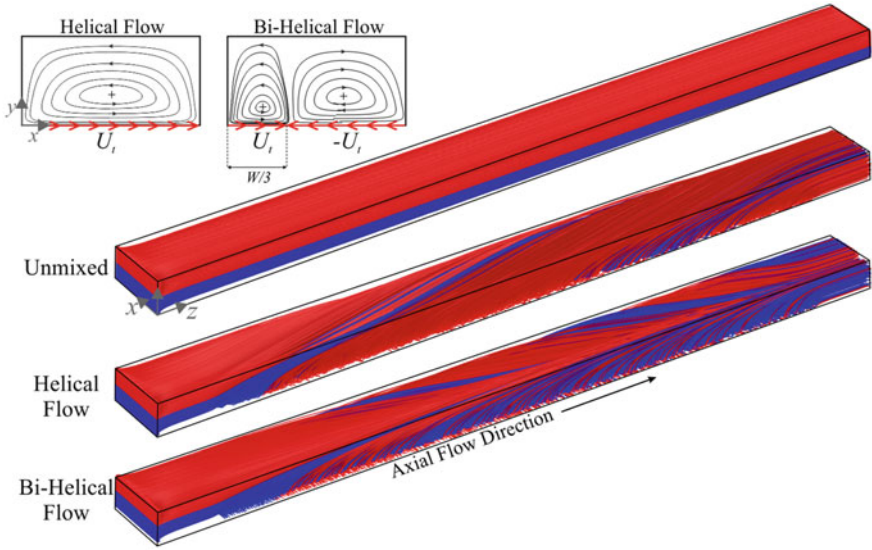


Fig. 4 Fluid mixing in a “lid-driven” microchannel, where three of the channel walls obey the no-slip condition and the channel floor moves with a velocity U_t (in the x -direction). For pressure-driven flow in the Stokes regime ($Re \ll 1$), the fluid velocity in the entire chamber can be sufficiently estimated by the superposition of axial Poiseuille flow (v_z , described by Eq. (3)) and a transverse flow profile v_t created from the moving wall. Cross-sectional streamlines (regarding v_t) for two types of fluid motion are shown in the upper left. Stagnation points for each flow profile are shown as the crosses. These simulations were performed with COMSOL, where $W = 2H$ and $U_t = U$

stretched and folded (in a manner similar to a baker’s transformation) such that fluid streamlines (and solutes) experience the entire cross-sectional space. For the mixers in Fig. 4, this can be achieved by alternating the helical and bi-helical flow profiles or more optimally, alternating sequences of the bi-helical flow with its mirror image (across x) [42].

A full discussion on chaotic mixing in laminar flows would require much more than the space available in this chapter. Thus, for now, we will disregard specific flow profiles and rather classify a mixer according to (i) it being either chaotic or non-chaotic and (ii) its characteristic transverse velocity U_t . Outside of the example shown in Fig. 4, U_t can be taken as the average magnitude of the fluid velocity in the x -direction.

3.1 Examination from a Local Perspective

Understandably, the equations listed in Table 2 are not valid when the fluid in the sensing chamber is mixed, and thus a different approach is required.

In order to characterize (and predict) the effect of mixing on analyte transport, it is useful to examine the problem from a local perspective. In this approach, we assume—for both unmixed and mixed channels—that rates of analyte transport to the entire sensing region can be sufficiently represented by $j_z = j_z(z)$, the analyte flux averaged across the width of the channel (along the x -direction). A *local* Sherwood number can then be defined as

$$\text{Sh}_z = \frac{k_m H}{D} = \frac{j_z H}{(c_b - c_s) D}, \quad (18)$$

where $k_m = k_m(z)$ is the local mass transfer coefficient, and $c_b = c_b(z)$ is the local (“mixing-cup”) analyte concentration,⁹ defined as

$$c_b(z) = \frac{\int_y \int_x c(x, y, z) v_z(y) dx dy}{UHW}. \quad (19)$$

The advantage of analysis from a local perspective is illustrated in Fig. 5a, which plots Sh_z as a function of the dimensionless axial distance $\bar{z} = z/\text{Pe}H$ for both mixed and unmixed channels; from Sect. 2.3, \bar{z} represents the inverse Graetz number. Under conditions spanning either phase (I) or (II), all sensors in an *unmixed* rectangular channel will exhibit the following trends:

- In the entrance region, where boundary layers remain small and $\bar{z} \ll 1$, the local Sherwood number will scale as $\text{Sh}_z \propto \bar{z}^{-1/3}$.
- In the fully developed region, where $\bar{z} \gtrsim 0.1$ and the boundary layer has filled the channel, the local Sherwood number will asymptotically approach a value of $\text{Sh}_\infty \approx 2.5$.

As noted by Kirtland et al. [46], sensors in *mixed* rectangular channels will exhibit similar trends:

- The rate of analyte transport in a mixed channel will be equivalent to that of an unmixed channel for axial distances of $z < z_\infty \approx WU/U_t$, where U_t is the characteristic transverse fluid velocity.
- For axial lengths of $z > z_\infty$, the local Sherwood number will deviate to an asymptotic value of $\text{Sh}_\infty \geq 2.5$. For sufficiently high values of Pe , this asymptotic Sherwood number will scale as $\text{Sh}_\infty \propto \text{Pe}_t^{1/3}$, where $\text{Pe}_t = \text{Pe}(U_t/U)$ is the transverse Péclet number.
- For *chaotically* mixed fluids in the asymptotic region ($z > z_\infty$), Sh_z will remain constant with increases in \bar{z} .
- For *non-chaotically* mixed fluids in the asymptotic region ($z > z_\infty$), there will be a decrease in Sh_z with increases in \bar{z} .

⁹The mixing-cup concentration c_b represents the concentration one would obtain by collecting the microchannel effluent with a small cup.

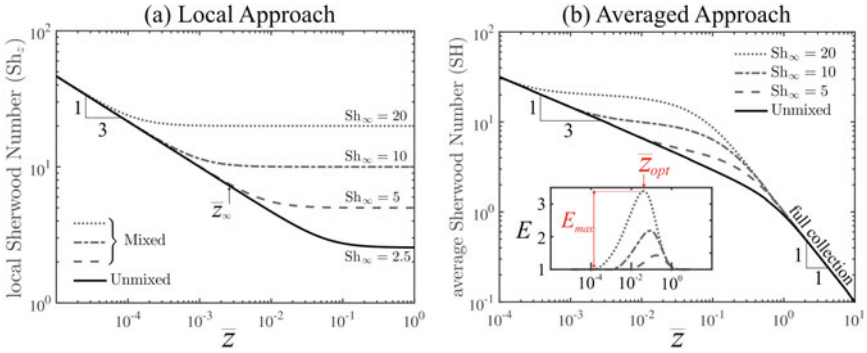


Fig. 5 Characteristic differences between unmixed and chaotically mixed sensors. **a** The local Sherwood number as a function of the dimensionless axial distance. Data for both the mixed and unmixed sensors were calculated from Eq. (20) using the respective values of Sh_∞ . **b** The macroscopic Sherwood number as a function of the dimensionless axial distance (L/PeH). These data were calculated from those shown in (a) via the use of Eqs. (14), (22), and (21). The inset shows E : the ratio of SH between the mixed and unmixed channels

For both unmixed and chaotically mixed fluids, the local Sherwood number can be sufficiently estimated in an analytical fashion as

$$Sh_z = (\bar{z}^{-5/3} + Sh_\infty^5)^{1/5}, \quad (20)$$

where it follows that $Sh_\infty = 2.5$ for an unmixed channel. It should be noted that Eq. (20) was not derived from first principles; rather, it represents a convenient method to estimate Sh_z analytically; this equation matches well to both data from FE simulations in unmixed channels (< 2% error) as well as random walk simulations in mixed channels [46, 47].

To put things in perspective, the data shown in in Fig. 5a might be representative of data taken from a variety of experimental situations, for example, (i) concerning an adjustable, chaotically mixed channel used for the detection of a single analyte at a single flow rate, increases in Sh_∞ would be a result of an increase in the magnitude of stirring (i.e., a higher U_t); or (ii) concerning a passive chaotic mixer (constant U_t/U), increases in Sh_∞ would be a result of either increasing the flow rate or similarly, the detection of analytes with progressively smaller diffusivities.

More information on the topic, including the behavior of non-chaotically mixed channels, can be found in [46, 48]. We also point the reader to a review of other topics related to transport phenomena within chaotic flows [49].

3.2 Prediction of Analyte Transport in Mixed Channels

Despite the convenience of an examination from a local approach, the results shown in Fig. 5a can be misleading to those not familiar with dimensionless analysis. For example, an increase in Sh_∞ by $10\times$ does not lead to a $10\times$ increase in the rate of mass transfer (either averaged across the sensor or measured at a specific axial distance corresponding to \bar{z}). As per the discussion regarding Eq. (13), it remains desirable to have information related to the average Sherwood number, which is directly related to experimental measurements. For such purposes, the local Sherwood number can be converted to a local flux as

$$j_z(z) = \frac{Sh_z(z)C_oD}{H} \exp\left(-\int_0^z \frac{Sh_z(z)}{PeH} dz\right), \quad (21)$$

where it follows that the average analyte flux can be calculated as

$$J = \frac{1}{L} \int_0^L j_z(z) dz, \quad (22)$$

which can be used directly with Eq. (14) to calculate SH (or likewise, to calculate $K_m = J/C_o$). Figure 5b displays the average Sherwood number as a function of the dimensionless axial distance for sensors of varying length; these data were calculated from those shown in Fig. 5a via Eqs. (21)–(22). The data for the unmixed sensor are equivalent to that given by Eq. (17).

The approach shown in Fig. 5 thus represents a convenient method to predict rates of mass transport to a sensing surface in chaotically mixed channels. Such predictions are relatively straightforward and follow a linear progression:

- (i) The asymptotic Sherwood number Sh_∞ can either be calculated numerically [46, 47] or for $Pe \gg 1$, be estimated as $Sh_\infty \approx (PeU_rH/UW)^{1/3}$ [49].
- (ii) The local Sherwood number $Sh_z(z)$ can then be estimated via Eq. (20).
- (iii) The average analyte flux J can then be estimated via Eqs. (21) and (22).
- (iv) If one has knowledge of the kinetic parameters, the average mass transfer coefficient $K_m = J/C_o$ can be used with Eq. 13 to estimate the rate of analyte collection as a function of time.

As demonstrated in Sect. 4.2, this approach can be used to provide accurate predictions of the transport behavior observed in experiment: specifically, in biosensors using both slanted [28] and herringbone grooves [50].

3.3 Scaling Behavior for Optimal Conditions

In order to discuss optimal mixing conditions for a biosensor, it is useful to compare how the rate of analyte capture in a mixed channel differs from that in an unmixed

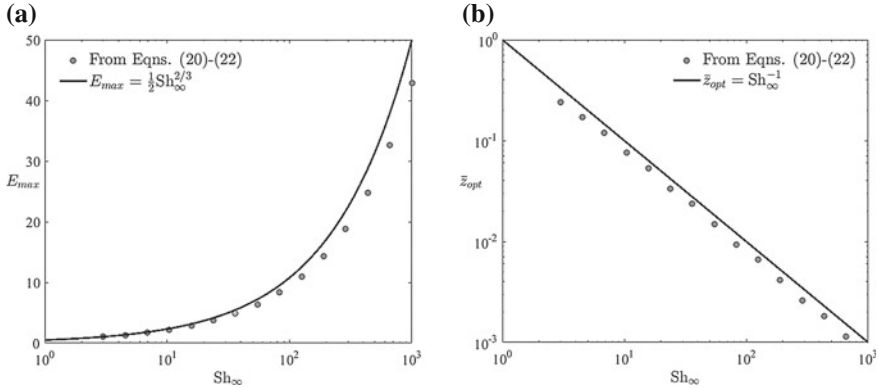


Fig. 6 Scaling behavior for optimal mixing conditions. The values E_{max} and \bar{z}_{opt} correspond to the positions of the maximum mixing enhancement E as shown in Fig. 5. The symbols were calculated from Eqs. (20)–(22) for both mixed channel (variable Sh_∞) and unmixed channels ($Sh_\infty = 2.5$)

channel. This comparison can be made through E , the ratio of SH (or equivalently K_m) between a mixed and unmixed sensor of similar dimension.¹⁰ This ratio—shown in the inset of Fig. 5b—is useful in highlighting several characteristics of how a chaotic mixing process affects the performance of a biosensor.

It is clear from the results in Fig. 5b that there is an optimal dimensionless axial distance, \bar{z}_{opt} , such that the effect of mixing will be maximized with an enhancement E_{max} . If a mixer is too short (i.e., $z < z_\infty$), the analyte collection rate will be equivalent to an unmixed channel; the same is true when a mixer is too long (i.e., $\bar{z} > 1$). From the perspective of maximizing J , optimal mixing conditions correspond to the distance at which a mixed channel reaches the limit of full collection (specifically, at the point where SH starts to scale as $SH \propto \bar{z}^{-1}$). It follows that this mixer length is also optimal in terms of the analyte collection efficiency.

We now have enough information to give a partial answer to question (B): what is the expected performance improvement that mixing can provide? A general answer to this question can be obtained by examining the scaling behavior of E_{max} , shown in Fig. 6a. It can be seen that, per Eqs. (20)–(22), this enhancement scales with the asymptotic (local) Sherwood number as $E_{max} \propto A_o Sh_\infty^{2/3}$, where $A_o \approx 0.5$. Knowing that the latter scales as $Sh_\infty \propto (PeU_i/U)^{1/3}$, it follows that the maximum sensing enhancement scales as $E_{max} \propto A_o (PeU_i/U)^{2/9}$.

It should be noted, however, that under many circumstances it may be difficult to realize the conditions leading to E_{max} . Referring to the results in Fig. 6b, the axial position corresponding to E_{max} is seen to scale as $\bar{z}_{opt} \propto Sh_\infty^{-1}$. In dimensional terms, the optimal length of a sensor will thus scale as $L_{opt} \propto H(U/U_i)^{1/3} Pe^{2/3}$.

¹⁰For quasi-steady, diffusion-limited conditions, the limit of detection for a mixed biosensor (LOD_m) is related to that of an unmixed biosensor (LOD) of similar dimension as $LOD_m = LOD \cdot E^{-1}$.

Applying these scaling results to one of our previous experimental studies [50], where a passive mixer was used to enhance the SPRi-based detection of bacteria ($H = 27 \mu\text{m}$, $U_i/U \approx 0.1$, and $\text{Pe} = 10^6$), we find that the maximum enhancement will follow $E_{max} \approx 6$; however, this maximum will require a mixer length of $L_{opt} \approx 581 \text{ mm}$! Such a length would likely present numerous experimental difficulties for a SPR-based sensor. Nevertheless, nonoptimal mixers can still provide benefits: under the same conditions, a mixer length of $L = 15 \text{ mm}$ was shown to have an enhancement of $E = 2.4$ [50].

It is also important to keep in mind that the value E represents the enhancement in analyte transport under diffusion-limited conditions. This value thus represents the upper bound of what can be experimentally realized: following Eq. 13, the actual level of enhancement due to mixing may be restricted by reaction limitations.

4 Experimental Applications: The Staggered Herringbone Mixer

The staggered herringbone mixer is perhaps the most notable example of a passive microfluidic mixer [26]. Illustrated in Fig. 7a, the SHM consists of herringbone-shaped grooves fabricated onto at least one wall of the microchannel. Under pressure-driven flow, these grooves generate two counter-rotating helical flows similar to that shown in Fig. 4, where alteration of the herringbone asymmetry along the channel length serves to mix the fluid in a chaotic fashion. For biosensing purposes, the SHM grooves are often placed on the wall opposite of the sensing region. Under proper conditions, the transverse bi-helical fluid motion can aid to increase the rate of analyte transport to a biosensor.

Since the seminal work on the topic, there have been a large number of analytical, numerical, and experimental studies focused on optimizing the traditional SHM geometry, a selected portion of which can be found in [51–56]. Additional works have focused on the optimization of mixing in SHM-like channels [57–60]. For readers of this chapter, however, caution must be taken in interpreting (or applying) the results of these studies, as they examine how changes to the SHM geometry affect the rate of mixing within the channel. For sensing applications, we are rather more interested in the rate of mass transfer to a sensing surface. These two end-use purposes (mixing and sensing) thus remain distinct; optimization of the first does not guarantee the same result for the second.

4.1 Optimization of the SHM Geometry for Biosensing

To date, only a limited number of studies have examined how changes in the SHM geometry affect analyte transport to a sensing surface. The initial study by Kirtland

et al. was pertinent in establishing many of the important concepts on the topic [46]; however, those results approximated flow in the SHM as being lid-driven [42], similar to that in Fig. 4, where axial fluid velocities remained unchanged along the length of the sensor. Consideration of the more complex SHM geometry requires a more detailed approach.

The complexity of analyte transport within a SHM is illustrated in Fig. 7a. Axial fluid velocities are higher in the thin channel regions between grooves, and lower in the regions under the grooves (where the effective channel height is larger). Transverse fluid velocities are even more intricate. The 3D flow profile leads to interweaved boundary layers and furthermore, a variable analyte flux profile that mirrors the groove design. Analyte flux is highest near the apex of each groove structure when the flow direction is aligned with the “points” of the herringbones, and lowest in the regions under the grooves.¹¹

From a numerical perspective, there is an inherent difficulty in studying analyte transport in the SHM. Accurate computation of fluid velocity fields in the SHM is possible with relatively modest computational resources; however, the computation of concentration fields is susceptible to numerical artifact, and accurate simulations require the use of unrealistic mesh densities [62]. For this reason, the contour and flux profiles shown in Fig. 7a cannot be used to obtain quantitative information.

A workaround to this computational problem was shown by Forbes and Kralj, who examined how changes in the herringbone geometry influence the frequency at which fluid streamlines come into proximity with the SHM surfaces [61]. As shown in Fig. 7b, they found that this streamline interaction frequency with *all* of the SHM surfaces is maximized when the hydraulic resistance of the grooves are equal to that of the channel. Thus, the sizes for both the channel (H) and groove height (h_g) can be used to analytically estimate the optimum groove width (w_g) without the need of computational simulation. Such a conclusion is certainly advantageous for SHM biosensors having all surfaces functionalized with bioreceptors. It is unclear if this approach is applicable toward the sensors considered in Fig. 7a, where only the surface opposite the grooves is functionalized. Although there is surely a relationship between the frequency of streamline interaction and the rate of analyte transport, the exact nature of that relationship is unknown.

An alternative method to estimate rates of analyte transport in the SHM is via the use of particle tracing simulations. These simulations, also used in the study by Kirtland et al. [46], are often applied to study mass transfer in complex domains [63]. We recently used these simulations to study analyte transport in the SHM [47]; examples of those results are shown in Fig. 7c. As expected, we found that (when averaged over each $1/2$ -cycle) the local Sherwood number deviates to an asymptotic value Sh_∞ that is dependent on both the Peclet number and more importantly, the geometry of the SHM. In general, we found that for a set microchannel height, increases in Sh_∞ can be obtained by decreasing W and increasing h_g , whereas changes in the groove pitch

¹¹When flow is reversed, the analyte flux is highest where the grooves meet the channel sidewalls. This arrangement is nonoptimal due to the lower axial velocities near the channel edges.

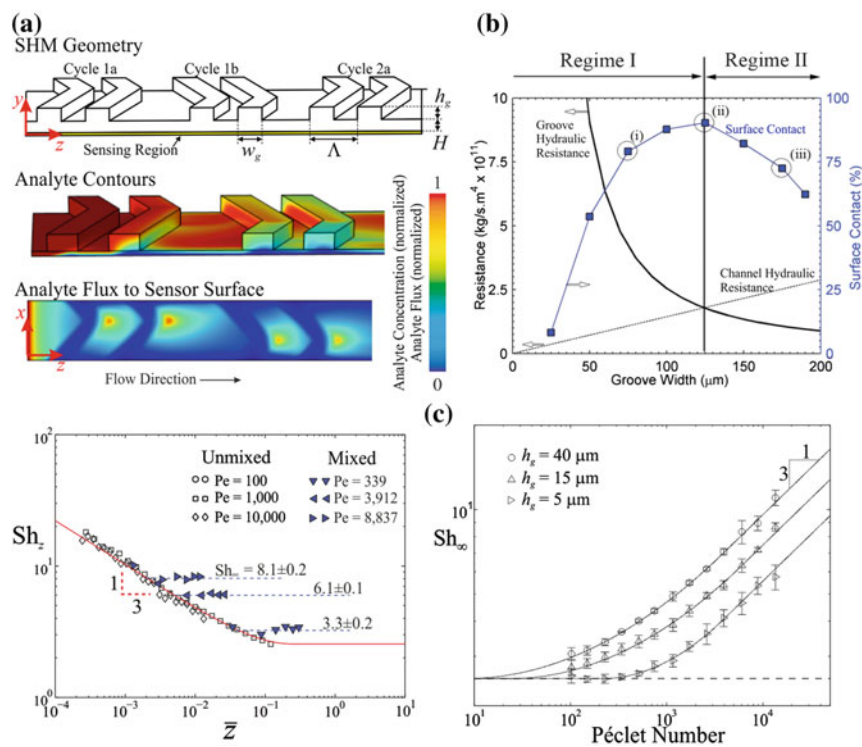


Fig. 7 **a** Schematic of the SHM geometry used for sensing purposes. Steady diffusion-limited analyte contours (normalized to C_o) and analyte flux contours (normalized by the maximum value) are shown for the first cycle (obtained via COMSOL) **b** Results from Forbes et al. [61]: the streamline surface contact with all surfaces of the SHM is maximized when the hydraulic resistance of the grooves (solid line) is equal to that of the channel (dashed line). **c** Results from Lynn et al. [47]: particle tracing simulations can be used to characterize the dimensionless behavior of a SHM; such behavior is similar to that in Fig. 5a (left). Increasing the groove depth (h_g) leads to increases in Sh_∞ (right), where increases in Pe for all channels lead to increases in Sh_g (Dimensional parameters in (c) were $H = 20 \mu\text{m}$, $W = 200 \mu\text{m}$, and $\Lambda = 150 \mu\text{m}$). The results in (b) were adapted from [61] with permission from the Royal Society of Chemistry. The results in (c) were adapted with permission from [47]. Copyright 2015 American Chemical Society

(Λ) and the number of grooves per $1/2$ -cycle (N_g) had little to no effect (the lack of dependence on Λ was also shown in [61]).

Using these simulations, we found that for an SHM with constant H and h_g there exists an optimal groove width such that Sh_∞ is maximized [47]. However, in contrast to the findings by Forbes and Kralj [61], this optimum groove width was not at the position of equal hydraulic resistance (as shown in Fig. 5b). To further complicate matters, we found that optimal groove widths (to maximize Sh_∞) were nonoptimal in terms of maximizing transverse fluid velocities.

Unfortunately, these previous studies cannot be used to formulate a “handbook” for the optimization of SHM-based biosensors. Nonetheless, there are a few guidelines that, while might not be optimal, can help improve a biosensor’s performance. Perhaps, the most important design tip is to simply increase the groove depth: a value of $h_g/H \approx 2$ seems to maximize Sh_∞ for all SHM geometries [47]. The other tip is to avoid the use of a single herringbone pattern over sufficiently wide channels: channels with symmetric herringbone patterns (with a symmetric width W_s) have a smaller effective width and thus serve to increase transport. As shown below, symmetric SHM designs are often used in experimental biosensors.

4.2 Experimental Use of the SHM for Biosensing

In the decade after the seminal work [26], there were only a few experimental studies utilizing the SHM for biosensing purposes. Most of the early reports pertained to the detection of analytes having relatively small sizes. To our knowledge, the first experimental use of a groove-based micromixer for biosensing purposes was reported by Golden et al., who used a mixer consisting of alternating sequences of slanted and v-grooves situated over a surface having immobilized bioreceptors [28]; below, we compare the results of this report with the discussion in Sect. 3 (*Case study 1*). For the second case study, we refer to one of our recent reports, where we used the SHM to enhance the detection of several analytes (ssDNA and *E. coli* bacteria) by a surface plasmon resonance imaging (SPRi) biosensor [50] (*Case study 2*).

Other reports on the topic for the detection of small analytes include that by Foley et al., who used a SPRi biosensor to characterize the spatial distribution of the capture of streptavidin under a channel composed of v-grooves [27]. Recently, Gomez-Aranzadi et al. demonstrated that SHM-based channels improve the capture rate of amine-coated polystyrene nanospheres (252 nm diameter) [64].

Comparison with Experiment: Case Study 1. The mixer used by Golden et al. [28] is shown in Fig. 8a.¹² The performance of this mixer was compared against an unmixed channel in two assay formats: (i) the direct detection of CY5-tagged biotin (with immobilized NeutrAvidin) and (ii) the detection of anti-botulinium toxin in a sandwich assay. The results for the direct detection assay are shown in Fig. 8a; the integrated fluorescent signal is proportional to the total number of analyte molecules captured from the beginning of the channel. They observed an increasing difference in fluorescence intensity between the mixed and unmixed channels along the length of the sensor. The mixed channel was observed to have a 26% higher fluorescence signal over the entire length of the channel ($L = 140$ mm).

The results shown by Golden et al. [28] represent a convenient example for comparison with the scaling behavior discussed in Sect. 3.3. Although their mixer did

¹²Reprinted from *Biosensors and Bioelectronics*, 22, Golden J.P., Floyd-Smith T.M., Mott D.R., and Ligler F.S., Target delivery in a microfluidic immunosensor, 2763-2767, 2007, with permission from Elsevier.

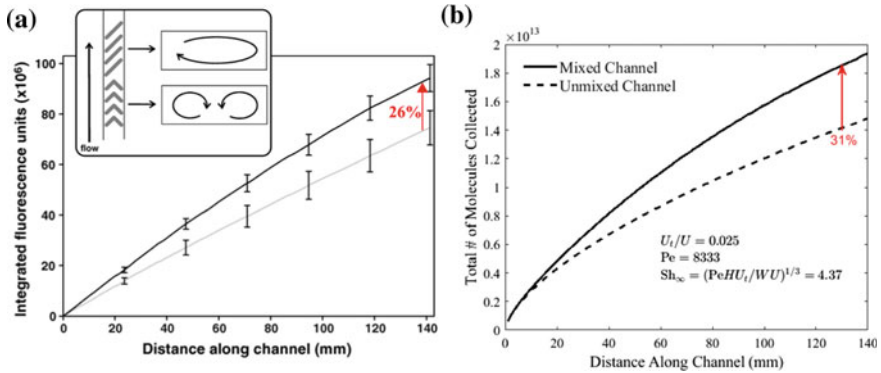


Fig. 8 **a** Results from Golden et al., adapted with permission from [28]: use of a grooved micromixer (shown schematically in the inset) for the direct detection of CY5-labeled biotin. Their mixer consisted of alternating sequences of v- and slanted-grooves. The plot shows the integrated fluorescence intensity as a function of axial distance for both mixed (black) and unmixed (gray) channels. Their channel had dimensions of $W = 200 \mu\text{m}$, $H = 80 \mu\text{m}$, and $h_g = 50 \mu\text{m}$. The flow rate was $Q = 1 \mu\text{L}/\text{min}$, and the assay proceeded for $t_a = 10 \text{ min}$. **b** Predictions of the total number of molecules bound as a function of axial distance for the results shown in [28]. The total number of molecules captured was calculated as $JWLt_a$, where J was calculated via Eqs. (20)–(22) ($Sh_\infty = 4.37$). The specific CY5-biotin marker was not given; however, using the respective sizes of CY5 and biotin, we estimated its diffusivity as $D \approx 10^{-10} \text{ m}^2 \text{ s}^{-1}$

not specifically use herringbone grooves, the use of alternating cycles of slanted and v-grooves represents the right “recipe” to create Lagrangian chaos [65]. Hence, we only need an estimate of Sh_∞ to predict the increase in analyte capture due to the inclusion of mixing. For an order of magnitude estimate, we can use their reported groove depth of $h_g/H = 0.625$ to estimate a transverse velocity ratio of $U_i/U \approx 0.025$ (via the results shown in [55]). From their reported flow conditions, we can estimate an order of magnitude estimate of $Sh_\infty \approx (PeU_iH/UW)^{1/3} \approx 4.37$, which leads to a maximum enhancement of $E_{max} \approx 1.34$ (34% enhancement) occurring at a channel length of $L \approx 112 \text{ mm}$ —values very close to those reported by the authors!

Taking our predictions one step further, we can apply our estimate of Sh_∞ to Eqs. (20)–(22) to estimate the total number of molecules captured by their sensor as $JLWt_a$, where t_a is the time of the assay. The results of this approach are shown in Fig. 8b. Comparison of our predicted values match very well with those shown in Fig. 8a. It should be stressed that there are undoubtedly some aspects that are overlooked in this predictive approach (e.g., equilibrium effects were not considered); however, the similarity in the results shown in Fig. 8 is quite impressive, especially considering that no numerical computation was required.

Comparison with Experiment: Case Study 2. In our previous study, we used a SPRi biosensor to monitor the direct detection of both ssDNA and *E. coli* bacteria, where detection was conducted over a range of flow rates and SHM designs. Because of the relatively large channel width, herringbone patterns were arranged in a sym-

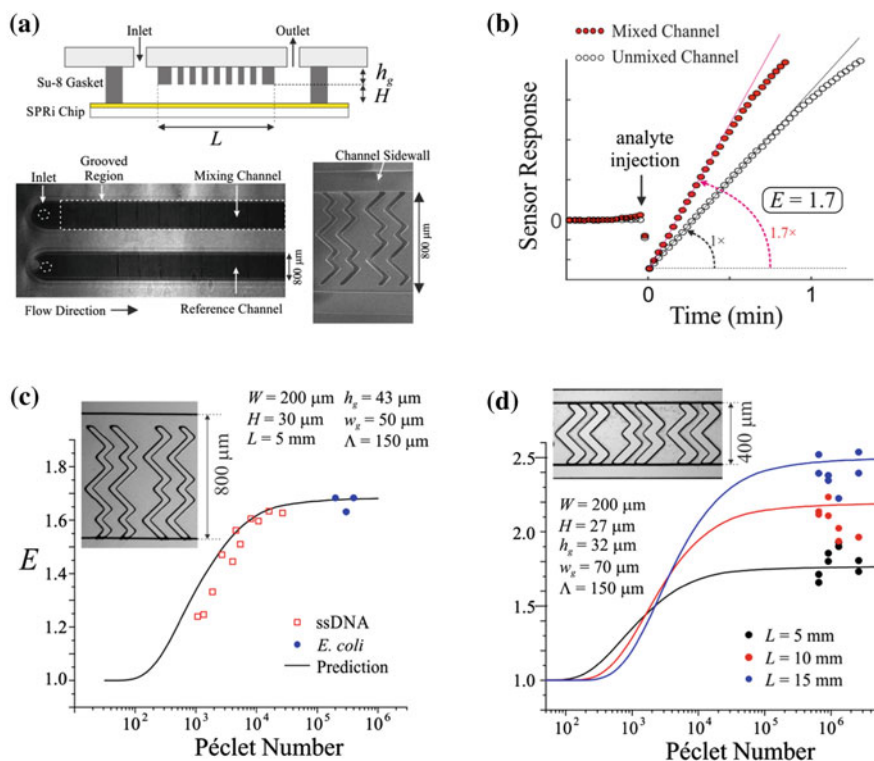


Fig. 9 Adapted with permission from [50]. Copyright 2015 American Chemical Society. **a** Schematic of the biosensor, which consisted of both mixed (SHM) and unmixed channels fabricated from Su8 and sealed to the SPRi chip. **b** Example sensor response in a mixed and unmixed channel for the detection of 20 b.p. ssDNA ($C_o = 20\ \text{nM}$). **c** and **d** Sensing enhancement E as a function of the Péclet number for the detection of both 20 b.p. ssDNA ($D = 9.9 \times 10^{-11}\ \text{m}^2\text{s}^{-1}$) and heat-killed $E. coli$ ($D = 3.2 \times 10^{-13}\ \text{m}^2\text{s}^{-1}$). The insets show light images of the SHM used in each experiment

metrical fashion; these patterns were optimized using the numerical methods in [47]. For each detection experiment, the performance increase due to the grooves was calculated by the ratio of initial binding rates between the SHM-mixed channel and an unmixed channel (Fig. 9b). Due to both the large difference in diffusivities between ssDNA and $E. coli$ as well as the wide range of flow rates ($5 < Q < 120\ \mu\text{L}/\text{min}$), the detection conditions in this case study spanned a wide range of Péclet numbers ($10^3 < Pe < 10^6$).

The effect of the Péclet number on the increase in sensor response due to mixing is shown in Fig. 9c, d. As expected from the discussion in Sect. 3.2, at sufficiently low Pe , there is no enhancement due to mixing, whereas increases in Pe result in a monotonic increase in E . The magnitude of such increase maintains a complex

dependency on both Sh_∞ and L ; as shown in Fig. 9d, increases in the latter result in higher sensing enhancements (for lengths such that $L < L_{opt}$).¹³

The data shown in Fig. 9 highlight the importance of the Péclet number on such mixed sensors. In general, if conditions are such that $Pe \lesssim 100$, mixing is not expected to provide any biosensing enhancement: a condition that remains applicable for sensors under severe mass transfer limitations (i.e., $Da \gg 1$). Mixing will provide the greatest benefit under conditions of very high Péclet number, where $Pe \gtrsim 10^5$. For smaller analytes, the required flow rates and channel sizes to meet these conditions are often undesirable. Conversely, these conditions are regularly encountered in microfluidic sensors for the detection of very large analytes, such as whole cell bacteria (as shown in Fig. 9) or circulating tumor cells.

4.3 Detection of Circulating Tumor Cells Using the SHM

Recently, there has been an increase in the use of the SHM-based biosensors for the detection of circulating tumor cells (CTCs). These cells are shed from cancerous tumors at rate such that their concentration in the bloodstream remains very low. The detection of these cells in a patient's bloodstream is thus an indicator of the presence of a primary tumor. Due to their low concentration, microfluidic approaches often aim toward maximizing the SHM capture efficiency, measured as the number of cells captured divided by the number of cells flown through the channel. There are currently several reviews on the microfluidic-based capture of CTCs, to which we refer the reader [66–71]. The diameters of relevant CTCs are in the order of $10\ \mu\text{m}$, which correlates to a diffusivity in aqueous media of $D \approx 10^{-14}\ \text{m}^2\text{s}^{-1}$ [71]. Thus, the detection of CTCs thus often corresponds to conditions in the range of $10^7 < Pe < 10^9$.

Use of all SHM surfaces for cell capture. The first use of the SHM for the detection of CTCs was reported by Stott et al. [29]. As shown in Fig. 10, they used an HB chip (consisting of eight SHM-based channels in series) to capture PC3 cells (a human prostate cancer cell) in whole blood. Unlike the model example shown in Fig. 1, bioreceptors were immobilized to all of the SHM surfaces. Using a scaled down single-channel device, the authors demonstrated that a SHM-mixed channel provided a markable increase in capture efficiency when compared to an unmixed channel developed in the previous study [72]. A decrease in flow rate resulted in an increase in capture efficiency for both mixed and unmixed channels (Fig. 10).

There have been since several reports on the use of the HB chip (either exactly as in [29] or with slight deviations in dimensions) for the detection of CTCs, where the entire SHM surface is used to capture CTCs. Sheng et al. used an HB chip to study the effect of various bioreceptors on the capture of CEM cells (a human leukemia T-cell)

¹³The scaling laws in Sect. 3.3 predict that there will be an indefinite increase in the *maximum* sensor enhancement E_{max} with increases in Pe ; however, this scaling law applies only to mixers of length L_{opt} .

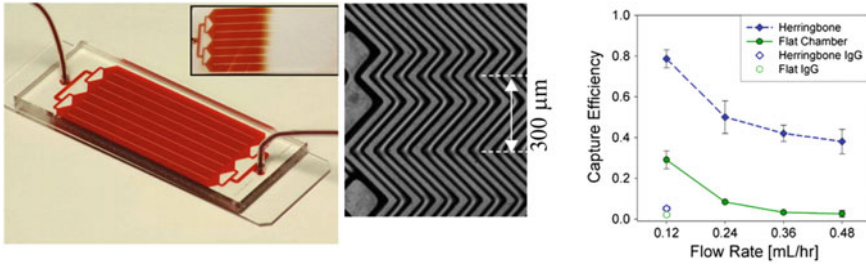


Fig. 10 Adapted with permission from Stott et al. [29]: **(left)** The HB chip consisted of a SHM channel fabricated from PDMS sealed to a glass slide. Bioreceptors (anti-EpCAM) were immobilized to both the glass and PDMS channel walls. Captured cells were detected using fluorescence microscopy. **(middle)** Symmetric placement of herringbone grooves (symmetric width $W_s = 300 \mu\text{m}$, $w_g = 50 \mu\text{m}$, $\Lambda = 100 \mu\text{m}$). **(right)** Capture efficiency of PC3 cells for both a SHM-based channel ($W = 2\text{mm}$, $h_g = 30 \mu\text{m}$, $H = 70 \mu\text{m}$, $L = 25 \mu\text{m}$) and an unmixed channel ($H = 100 \mu\text{m}$) as a function of the flow rate through a smaller, single-channel device. Also shown is the capture efficiency of IgG

[73]; they showed that bioreceptors consisting of aptamer-coated gold nanoparticles performed significantly better than both aptamers alone (no nanoparticles) as well as anti-PTK7 antibodies. A pair of studies by Xue et al. used both the original HB chip [74] and a modified HB chip [75] (with posts opposite to the grooves) to capture Hep3B cells (human liver cancer cells, anti-EpCAM bioreceptors). A device by Liu et al. used enrichment channels to separate MCF7 cells from other blood cells (using deterministic lateral displacement [76]), which were subsequently captured by a SHM-based channel [77]. A follow-up study by the same authors demonstrated that changing the dimensions of the herringbone grooves (in accordance with the results of Forbes and Kralj [61]) resulted in both a slight increase in capture efficiency as well as a large increase in the capture purity (measured as the number of targeted versus total cells captured) [73].

In another study using the results of Forbes and Kralj [61] to optimize the HB chip, Hyun et al. studied the effect of several SHM designs on the capture efficiency of Jurkat cells (a human T-cell lymphoblast cell line) [78]. The three different SHM designs used in their study are shown in Fig. 11. In comparison to the design by Stott et al. [29], they showed that increases in capture efficiency can be obtained by increasing the groove width w_g (constant W_s). Further increases were obtained by decreasing W_s , which is in accordance with the results in [47] (albeit for a single surface).

A note regarding transport in “all-surface” SHM channels. An analysis of transport in SHM channels using all surfaces for capture requires a slightly different approach from the discussion in Sect. 3.2.¹⁴ In a follow-up study to their seminal work, Kirtland et al. demonstrated that for a chaotic lid-driven micromixer (Fig. 4), the asymp-

¹⁴For *unmixed* flow in wide channels, the asymptotic local Sherwood number is $Sh_\infty \approx 7.5$ [79] and furthermore, the integral in Eq. (21) is multiplied by a factor of 2 into account for the additional reactive surface.

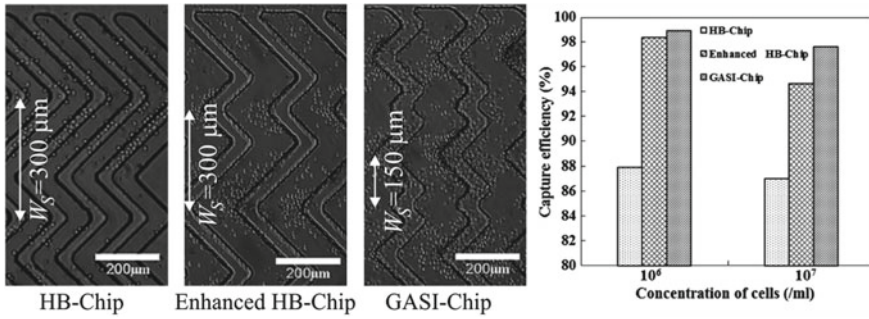


Fig. 11 Adapted with permission from [78]. Copyright 2013 American Chemical Society: capture of Jurkat cells by a SHM. Their HB chip used similar dimensions as [29] ($W = 2.1$ mm, $L = 50$ mm, $H = 50$ μ m, $h_g = 45$ μ m, $w_g \approx 50$ μ m, $\Lambda = 100$ μ m). The enhanced HB chip was designed using the results found in [61] and applied to the HB chip keeping W_s constant ($h_g = 50$ μ m, $w_g = 125$ μ m, and $\Lambda = 200$ μ m). The GASI chip used a decreased herringbone width. The capture efficiency was measured for all three chips at two cell concentrations

otic local Sherwood number for the *moving* wall scales as $Sh_\infty \propto (PeU_t/U)^{1/2}$ [48]. As mentioned previously, the lid-driven mixer has previously been shown to emulate flow in the SHM [42]; however, it is unclear if this scaling relationship holds for the SHM geometry, where the grooves themselves are stationary. To our knowledge, there are currently no methods to predict how the capture efficiency of these sensors is dependent on either the SHM architecture or the operating conditions.

Case Study 3: Use of a single SHM surface for cell capture. Another early use of the SHM for CTC detection was shown by Wang et al. [80]. Contrary to the previous studies, where all of the SHM surfaces were active in CTC capture, the device used in [80] had immobilized bioreceptors only on the surface opposite the SHM grooves. Hence, we use this as our third case study for comparison to the predictive approach in Sect. 3.2.

The device in [80] consisted of a wandering SHM used for the capture of MCF7 cells (a human breast cancer cell) onto a nanostructured surface consisting of silicon nanopillars (SiNPs). Their device was shown to have a capture efficiency of $> 95\%$ for flow rates up to 2 mL h^{-1} , where similar to [29], they observed a drop in capture efficiency at higher flow rates (down to $\approx 30\%$ at 7 mL h^{-1}). An unmixed channel had a capture efficiency of $\approx 60\%$ (1 mL h^{-1}).

Similar devices have since been used by the same authors for (i) the capture of other CTCs (SKBR3 cells, anti-EpCAM bioreceptors) and subsequent analysis by laser capture microdissection (LCM) [81], (ii) the capture and LCM analysis of circulating melanoma cells (CMCs) (anti-CD146 bioreceptors) [82], and (iii) the capture of A549 cells (human lung cancer) via immobilized aptamers [83]. Reported capture efficiencies for these studies were similar to that in [80].

The previous two case studies pertained to the detection of analytes having relatively well-defined sizes. Conversely, MCF7 cells have been shown to have a large size distribution, with cell radii measured to be $r_c = 9.6 \pm 4.2$ μ m [85]. For purposes

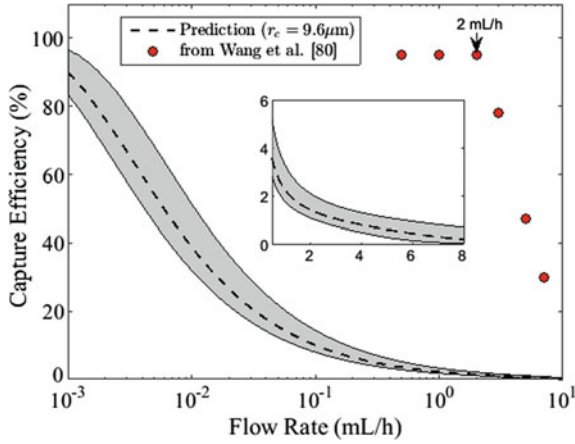


Fig. 12 Comparison of the data in [80]. SHM dimensions were reported as $W = 1$ mm, $H = 100$ μ m, $L = 880$ mm, $h_g = 35$ μ m, $w_g = 35$ μ m, and $\Lambda = 100$ μ m. The reported groove depth of $h_g/H = 0.35$ was used to estimate $U_t/U = 0.02$ [55], where we assumed $Sh_\infty = (PeU_tH/UW)^{1/3}$. Predictions of capture efficiency were calculated as $JLW/QC_o \cdot 100$, where J was calculated using Eqs. (20)–(22). The dashed line pertains to predictions regarding cells of size $r_c = 9.6$ μ m. The upper and lower bounds of the shaded area pertain to cells of $r_c = 5.4$ and 13.8 μ m, respectively. Diffusivities were calculated via the Einstein–Stokes relationship at 25C, where the viscosity of the DMEM medium was taken to be $\mu = 0.94$ cP [84]. Data representative of [80] is shown in the red symbols

of prediction, it is reasonable to assume that the average rate of transport for a distribution of cell sizes is bound by that for fixed distributions of cells having sizes on the upper and lower ends of what is experimentally observed; we take such an approach here.

Figure 12 shows the predicted capture efficiency as a function of the flow rate for the conditions described in [80]. In terms of J , the capture efficiency can be taken as the rate of cells captured by the sensor (JLW) divided by the rate of cells entering the channel (QC_o) times 100.

In contrast to the previous two case studies, predictions via Eqs. (20)–(22) do not match well with the observed experimental behavior in [80] for the capture of CTCs. At a flow rate of $Q = 1$ mL h⁻¹, the predicted upper and lower bounds for the capture efficiency are 3.3% and 1.8%, respectively. These low values cannot be attributed to errors in estimating U_t ; a much larger (and experimentally unreasonable) value of $U_t/U = 1$ leads to a capture efficiency of 7.7% ($r_c = 9.6$ μ m, $Q = 1$ mL h⁻¹). Factors contributing to these discrepancies are discussed in the next section.

4.4 Prediction of CTC Capture: Factors to Consider

The discrepancies between the predicted and experimentally observed transport behavior of CTCs in mixed channels (Fig. 12) can primarily be attributed to the large size of the CTCs with respect to the smaller analytes considered in Figs. 8 and 9. The relatively large size of a CTC with respect to that of a microchannel affects transport behavior through a variety of mechanisms.

One source of discrepancy is that under certain conditions a CTC might not follow the fluid streamlines in a microchannel, that is, where inertial forces become greater than the drag force of the fluid. The relative magnitude between these two forces can be estimated (in dimensionless fashion) by the Stokes number (St):

$$\text{St} = \frac{2\rho_c U_o r_c^2}{9\mu H}, \quad (23)$$

where ρ_c is the CTC mass density, and we have taken the channel height to be the characteristic “obstacle size”. A cell can be considered to follow a fluid streamline for conditions such that $\text{St} \ll 1$, where drag forces become dominant. Taking the mass density of MCF7 cells to be $\rho_c = 1.04 \rho$ [86], we can estimate this value for the results shown in Fig. 12 as $\text{St} \approx 0.6$ ($Q = 1 \text{ mL h}^{-1}$). Thus, the advection of cells at this flow rate (and higher) cannot be assumed to precisely follow fluid streamlines throughout the chamber.

Aside from inertial effects, the parabolic nature of pressure-driven flow can influence a CTC in several ways. Sufficiently large cells (with respect to H) can be subjected to a large range in fluid velocities across the length of the cell. Cells close to a channel surface experience significant shear forces, which may damage cells and prevent cell capture [87]. Furthermore, cells in the center of a channel can have velocities much smaller with respect to the fluid velocity if no cell were present [88]; this effect would be significant for a CTC flowing within a herringbone groove. It is unclear if either of these effects contribute to the discrepancies shown in Fig. 12.

Perhaps, the most important source of discrepancy is the effect of cell settling caused by the difference in the mass density between cell and fluid. The settling velocity of a spherical cell in a static flow field can be taken from Stokes’ law as

$$v_s = \frac{2(\rho_c - \rho)Gr_c^2}{9\mu}, \quad (24)$$

where G is the gravitational constant. Applying this to the size distribution found in MCF7 cells ($r_c = 9.6 \pm 4.2 \mu\text{m}$) leads to estimated settling velocities in the range of $2.7 < v_s < 17.7 \text{ mm/s}$. In comparison, the experimental conditions in [80] correspond to axial fluid velocities in the range of $1.4 < U < 19.4 \text{ mm/s}$. Although there are other factors that must be considered (e.g., inertial effects from the helical flow field, deformability of the CTCs), the settling of CTCs is likely to have lead to increased rates of capture when compared to a pure convection and diffusion

approach as discussed in Sect. 3.2. This effect was also noted by Stott et al. to have an influence on CTC capture [29]; however, no details were given on the frequency of cells captured by the upper and lower microchannel surfaces.

Although not relevant to Fig. 12, another factor to consider is the viscous nature of the detection media. For example, whole blood is shear thinning, where fluid viscosities at high shear rates are over an order of magnitude lower with respect to viscosities at static conditions [89]. Thus, the diffusivity of CTCs (or any other analyte) cannot be considered to be constant across the channel height,¹⁵ where from a microscopic perspective, fluid shear is zero at the channel center and maximized at the channel walls.

The combined effects from these factors thus serve to muddy the predictive approach discussed herein. It is clear that such an approach has a good match when applied to the detection of smaller analytes; however, as demonstrated in Fig. 12, the same cannot be said regarding the larger CTCs.

In a similar fashion, these additional effects also pertain to the streamline-based approach shown by Forbes and Kralj [61]. Although their approach is certainly useful—as evidenced by the results of several experimental reports [73, 78]—questions remain if those positive results were a result of other factors: increased fluid streamline contact does not always imply increased CTC contact.

Nonetheless, there still remains a large gap in the literature on this topic, regardless of what SHM surface is doing the capture.

5 Final Notes

Although there has been a vast deal of work on the design and implementation of microfluidic mixers, their direct use with a biosensing process has been relatively limited. An obvious reason for this seems to lie in the technical complexity of the task: taken separately, both biosensing and micromixing are complicated processes, and the number of issues to troubleshoot when simultaneously considering both does not scale linearly. On the other hand, one must wonder how many researchers were successful in incorporating the two devices with one another, yet were unable to find any “interesting” results for mixed channels. As per the discussion above, there is a wide range of conditions for when mixing will *not* be beneficial to a biosensor. Many of these conditions are relatively unintuitive, even to those who have backgrounds in transport phenomena.

So when is mixing worth the trouble? A nontechnical answer is that the sensing region needs to be sufficiently long, such that the effect of mixing is realized, and furthermore, flow rates need to be sufficiently fast, such that analyte transport is dominated by convection and detection is far from being limited by interaction kinetics. Referring back to Sect. 2, these conditions are better stated in dimensionless terms,

¹⁵From the Einstein–Stokes equation, the diffusivity of an analyte is inversely proportional to the fluid viscosity.

where conditions should be such that $Pe \gg 1$, $Pe > \eta$, and $Da \gg 1$. Although far from being precise, another rule of thumb condition should be $\eta > 1$. In general, sensing conditions outside these bounds will remain unaffected by any microfluidic mixing process.¹⁶

And how much benefit can mixing provide? The upper bounds of this question can be estimated as $E_{max} \approx 1/2(PeU_i/U)^{2/9}$, which is valid for a mixer having a length of $L_{opt} \approx H(U/U_i)^{1/3}Pe^{2/3}$. Thus, mixing will be most beneficial for the detection of analytes having low diffusivity in channels that are (from a biosensing perspective) relatively long. The discussion in Sect. 3.2 provides a relatively simple method that one can use to predict the mass transfer response of a biosensor in a mixed channel. As per the results shown in Figs. 8 and 9, this method can be used with confidence for the detection of sufficiently small analytes.

The vast majority of the experimental literature on the topic herein involves the use of the staggered herringbone mixer to increase the rate of CTC capture. In contrast to smaller analytes, there are several transport mechanisms that become dominant due to the large size of the CTC, and the methods discussed in Sect. 3.2 lead to erroneous predictions. Owing to the importance of the problem, further study on the transport of CTCs in mixed channels would certainly be beneficial.

We hope that the reader finds this chapter useful in elucidating the complex behavior involved in coupling a biosensor with a microfluidic mixer. We encourage the reader to explore the preceding works on the topic [15, 46, 48, 49], which, despite their complexity, are useful for researchers in a variety of fields. This chapter represents an attempt to translate those works into the language used by those in the biosensing community.

Acknowledgements The authors would like to acknowledge funding from both the Praemium Academiae of the Academy of Sciences of the Czech Republic as well as the Czech Science Foundation (contract no. P205/12/G118).

References

1. Luka G, Ahmadi A, Najjaran H, Alocilja E, DeRosa M, Wolthers K, Malki A, Aziz H, Althani A, Hoorfar M (2015) Microfluidics integrated biosensors: a leading technology towards lab-on-a-chip and sensing applications. *Sensors* 15(12):30011–30031
2. Estevez M-C, Alvarez M, Lechuga LM (2012) Integrated optical devices for lab-on-a-chip biosensing applications. *Laser Photonics Rev* 6(4):463–487
3. Homola J (2008) Surface plasmon resonance sensors for detection of chemical and biological species. *Chem Rev* 108(2):462–493
4. White IM, Yazdi SH, Wei WY (2012) Optofluidic sers: synergizing photonics and microfluidics for chemical and biological analysis. *Microfluid Nanofluid* 13(2):205–216
5. Rackus DG, Shamsi MH, Wheeler AR (2015) Electrochemistry, biosensors and microfluidics: a convergence of fields. *Chem Soc Rev* 44(15):5320–5340

¹⁶This applies for mixing in the sense as shown in Fig. 1, where there is no selective transport specific to the analyte (e.g., (di)electrophoresis, thermophoresis).

6. Reverté L, Prieto-Simón B, Campàs M (2016) New advances in electrochemical biosensors for the detection of toxins: nanomaterials, magnetic beads and microfluidics systems. a review. *Anal Chim Acta* 908:8–21
7. Sang S, Zhao Y, Zhang W, Li P, Hu J, Li G (2014) Surface stress-based biosensors. *Biosens Bioelectron* 51:124–135
8. Skládal P (2016) Piezoelectric biosensors. *TrAC Trends Anal Chem* 79:127–133
9. Yakovleva M, Bhand S, Danielsson B (2013) The enzyme thermistor: a realistic biosensor concept. A critical review. *Anal Chimica Acta* 766:1–12
10. Wang T, Zhou Y, Lei C, Luo J, Xie S, Pu H (2016) Magnetic impedance biosensor: a review. *Biosens Bioelectron*
11. Faustino V, Catarino SO, Lima R, Minas G (2015) Biomedical microfluidic devices by using low-cost fabrication techniques: a review. *J Biomech*
12. Whitesides GM (2006) The origins and the future of microfluidics. *Nature* 442(7101):368–373
13. Squires TM, Quake SR (2005) Microfluidics: fluid physics at the nanoliter scale. *Rev Mod Phys* 77(3):977
14. Stone HA, Stroock AD, Ajdari A (2004) Engineering flows in small devices: microfluidics toward a lab-on-a-chip. *Annu Rev Fluid Mech* 36:381–411
15. Squires TM, Messinger RJ, Manalis SR (2008) Making it stick: convection, reaction and diffusion in surface-based biosensors. *Nat Biotechnol* 26(4):417–426
16. Lynn NS, Šípová H, Adam P, Homola J (2013) Enhancement of affinity-based biosensors: effect of sensing chamber geometry on sensitivity. *Lab Chip* 13(7):1413–1421
17. Hofmann O, Voirin G, Niedermann P, Manz A (2002) Three-dimensional microfluidic confinement for efficient sample delivery to biosensor surfaces. Application to immunoassays on planar optical waveguides. *Anal Chem* 74(20):5243–5250
18. Yoon SK, Fichtl GW, Kenis PJ (2006) Active control of the depletion boundary layers in microfluidic electrochemical reactors. *Lab Chip* 6(12):1516–1524
19. Mokrani A, Castelain C, Peerhossaini H (1997) The effects of chaotic advection on heat transfer. *Int J Heat Mass Transf* 40(13):3089–3104
20. Jana S, Ottino J (1992) Chaos-enhanced transport in cellular flows. *Philosophical transactions of the Royal Society of London a: mathematical. Phys Eng Sci* 338(1651):519–532
21. Hessel V, Löwe H, Schönfeld F (2005) Micromixers: a review on passive and active mixing principles. *Chem Eng Sci* 60(8):2479–2501
22. Chang C-C, Yang R-J (2007) Electrokinetic mixing in microfluidic systems. *Microfluid Nanofluid* 3(5):501–525
23. Ottino JM, Wiggins S (2004) Introduction: mixing in microfluidics. *Philos Trans Math Phys Eng Sci* pp. 923–935,
24. Lee C-Y, Wang W-T, Liu C-C, Fu L-M (2016) Passive mixers in microfluidic systems: a review. *Chem Eng J* 288:146–160
25. Ward K, Fan ZH (2015) Mixing in microfluidic devices and enhancement methods. *J Micromech Microeng* 25(9):094001
26. Stroock AD, Dertinger SK, Ajdari A, Mezić I, Stone HA, Whitesides GM (2002) Chaotic mixer for microchannels. *Science* 295(5555):647–651
27. Foley JO, Mashadi-Hosseini A, Fu E, Finlayson BA, Yager P (2008) Experimental and model investigation of the time-dependent 2-dimensional distribution of binding in a herringbone microchannel. *Lab Chip* 8(4):557–564
28. Golden JP, Floyd-Smith TM, Mott DR, Ligler FS (2007) Target delivery in a microfluidic immunosensor. *Biosens Bioelectron* 22(11):2763–2767
29. Stott SL, Hsu C-H, Tsukrov DI, Yu M, Miyamoto DT, Waltman BA, Rothenberg SM, Shah AM, Smas ME, Korir GK et al (2010) Isolation of circulating tumor cells using a microvortex-generating herringbone-chip. *Proc Natl Acad Sci* 107(43):18392–18397
30. McPeak KM, Baxter JB (2009) Zn nanowires grown by chemical bath deposition in a continuous flow microreactor. *Cryst Growth Des* 9(10):4538–4545
31. Khinast JG, Bauer A, Bolz D, Panarello A (2003) Mass-transfer enhancement by static mixers in a wall-coated catalytic reactor. *Chem Eng Sci* 58(3):1063–1070

32. Isfahani RN, Bigham S, Mortazavi M, Wei X, Moghaddam S (2015) Impact of micromixing on performance of a membrane-based absorber. *Energy* 90:997–1004
33. Myszka DG, He X, Dembo M, Morton TA, Goldstein B (1998) Extending the range of rate constants available from biacore: interpreting mass transport-influenced binding data. *Biophys J* 75(2):583–594
34. Eddowes M (1987) Direct immunochemical sensing: basic chemical principles and fundamental limitations. *Biosensors* 3(1):1–15
35. Glaser RW (1993) Antigen-antibody binding and mass transport by convection and diffusion to a surface: a two-dimensional computer model of binding and dissociation kinetics. *Anal Biochem* 213(1):152–161
36. Biacore A (1997) Biaevaluation software handbook, version 3.0. Biacore AB, Uppsala, Sweden
37. Newman J (1973) The fundamental principles of current distribution and mass transport in electrochemical cells. *Electroanal Chem* 6:279–297
38. Ackerberg R, Patel R, Gupta S (1978) The heat/mass transfer to a finite strip at small Péclet numbers. *J Fluid Mech* 86(01):49–65
39. Zhang W, Stone H, Sherwood J (1996) Mass transfer at a microelectrode in channel flow. *J Phys Chem* 100(22):9462–9464
40. Lynn NSS Jr, Homola J (2016) (bio) sensing using nanoparticle arrays: on the effect of analyte transport on sensitivity. *Anal Chem* 88(24):12145–12151
41. Lynn NS, Henry CS, Dandy DS (2008) Microfluidic mixing via transverse electrokinetic effects in a planar microchannel. *Microfluid Nanofluid* 5(4):493–505
42. Stroock AD, McGraw GJ (2004) Investigation of the staggered herringbone mixer with a simple analytical model. *Philosophical transactions of the Royal Society of London a: mathematical. Phys Eng Sci* 362(1818):971–986
43. Wiggins S, Ottino JM (2004) Foundations of chaotic mixing. *Philosophical transactions of the Royal Society of London a: mathematical. Phys Eng Sci* 362(1818):937–970
44. Ottino JM (1989) *The kinematics of mixing: stretching, chaos, and transport*, vol. 3. Cambridge University Press
45. Ottino J (1990) Mixing, chaotic advection, and turbulence. *Annu Rev Fluid Mech* 22(1):207–254
46. Kirtland JD, McGraw GJ, Stroock AD (2006) Mass transfer to reactive boundaries from steady three-dimensional flows in microchannels. *Phys Fluids* 18(7):073602 (1994–present)
47. Lynn NS Jr, Homola J (2015) Biosensor enhancement using grooved micromixers: Part i, numerical studies. *Anal Chem* 87(11):5516–5523
48. Kirtland JD, Siegel CR, Stroock AD (2009) Interfacial mass transport in steady three-dimensional flows in microchannels. *New J Phys* 11(7):075028
49. Sundararajan P, Stroock AD (2012) Transport phenomena in chaotic laminar flows. *Annu Rev Chem Biomol Eng* 3:473–496
50. Lynn NS Jr, Bockova M, Adam P, Homola J (2015) Biosensor enhancement using grooved micromixers: part ii, experimental studies. *Anal Chem* 87(11):5524–5530
51. Kang TG, Kwon TH (2004) Colored particle tracking method for mixing analysis of chaotic micromixers. *J Micromech Microeng* 14(7):891
52. Aubin J, Fletcher DF, Xuereb C (2005) Design of micromixers using cfd modelling. *Chem Eng Sci* 60(8):2503–2516
53. Yang J-T, Huang K-J, Lin Y-C (2005) Geometric effects on fluid mixing in passive grooved micromixers. *Lab Chip* 5(10):1140–1147
54. Hassell D, Zimmerman W (2006) Investigation of the convective motion through a staggered herringbone micromixer at low reynolds number flow. *Chem Eng Sci* 61(9):2977–2985
55. Lynn NS, Dandy DS (2007) Geometrical optimization of helical flow in grooved micromixers. *Lab Chip* 7(5):580–587
56. Yun S, Lim G, Kang KH, Suh YK (2013) Geometric effects on lateral transport induced by slanted grooves in a microchannel at a low reynolds number. *Chem Eng Sci* 104:82–92
57. Kim DS, Lee SW, Kwon TH, Lee SS (2004) A barrier embedded chaotic micromixer. *J Micromech Microeng* 14(6):798

58. Sato H, Ito S, Tajima K, Orimoto N, Shoji S (2005) Pdms microchannels with slanted grooves embedded in three walls to realize efficient spiral flow. *Sens Actuators A Phys* 119(2):365–371
59. Jain M, Rao A, Nandakumar K (2013) Numerical study on shape optimization of groove micromixers. *Microfluid Nanofluid* 15(5):689–699
60. Liu Y, Deng Y, Zhang P, Liu Z, Wu Y (2013) Experimental investigation of passive micromixers conceptual design using the layout optimization method. *J Micromech Microeng* 23(7):075002
61. Forbes TP, Kralj JG (2012) Engineering and analysis of surface interactions in a microfluidic herringbone micromixer. *Lab Chip* 12(15):2634–2637
62. Wesseling P (2009) Principles of computational fluid dynamics, vol 29. Springer Science & Business Media
63. Salamon P, Fernández-García D, Gómez-Hernández J (2006) Modeling mass transfer processes using random walk particle tracking. *Water Resour Res* 42(11)
64. Gomez-Aranzadi M, Arana S, Mujika M, Hansford D (2015) Integrated microstructures to improve surface-sample interaction in planar biosensors. *IEEE Sens J* 15(2):1216–1223
65. Aref H (1984) Stirring by chaotic advection. *J Fluid Mech* 143:1–21
66. Dong Y, Skelley AM, Merdek KD, Sprott KM, Jiang C, Pierceall WE, Lin J, Stocum M, Carney WP, Smirnov DA (2013) Microfluidics and circulating tumor cells. *J Mol Diagn* 15(2):149–157
67. Hajba L, Guttman A (2014) Circulating tumor-cell detection and capture using microfluidic devices. *TrAC Trends Anal Chem* 59:9–16
68. Miyamoto DT, Sequist LV, Lee RJ (2014) Circulating tumour cells [mdash] monitoring treatment response in prostate cancer. *Nat Rev Clin Oncol* 11(7):401–412
69. Murlidhar V, Rivera-Báez L, Nagrath S (2016) Affinity versus label-free isolation of circulating tumor cells: who wins?. *Small*
70. Qian W, Zhang Y, Chen W (2015) Capturing cancer: emerging microfluidic technologies for the capture and characterization of circulating tumor cells. *Small* 11(32):3850–3872
71. Smith JP, Barbati AC, Santana SM, Gleghorn JP, Kirby BJ (2012) Microfluidic transport in microdevices for rare cell capture. *Electrophoresis* 33(21):3133–3142
72. Nagrath S, Sequist LV, Maheswaran S, Bell DW, Irimia D, Utkus L, Smith MR, Kwak EL, Digumarthy S, Muzikansky A et al (2007) Isolation of rare circulating tumour cells in cancer patients by microchip technology. *Nature* 450(7173):1235–1239
73. Sheng W, Ogunwobi OO, Chen T, Zhang J, George TJ, Liu C, Fan ZH (2014) Capture, release and culture of circulating tumor cells from pancreatic cancer patients using an enhanced mixing chip. *Lab Chip* 14(1):89–98
74. Xue P, Ye K, Gao J, Wu Y, Guo J, Hui KM, Kang Y (2014) Isolation and elution of hep3b circulating tumor cells using a dual-functional herringbone chip. *Microfluid Nanofluid* 16(3):605–612
75. Xue P, Wu Y, Guo J, Kang Y (2015) Highly efficient capture and harvest of circulating tumor cells on a microfluidic chip integrated with herringbone and micropost arrays. *Biomed Microdevices* 17(2):1–8
76. Huang LR, Cox EC, Austin RH, Sturm JC (2004) Continuous particle separation through deterministic lateral displacement. *Science* 304(5673):987–990
77. Liu Z, Zhang W, Huang F, Feng H, Shu W, Xu X, Chen Y (2013) High throughput capture of circulating tumor cells using an integrated microfluidic system. *Biosens Bioelectron* 47:113–119
78. Hyun K-A, Lee TY, Jung H-I (2013) Negative enrichment of circulating tumor cells using a geometrically activated surface interaction chip. *Anal Chem* 85(9):4439–4445
79. Bird RB, Stewart WE, Lightfoot EN (2007) Transport phenomena. Wiley
80. Wang S, Liu K, Liu J, Yu ZT-F, Xu X, Zhao L, Lee T, Lee EK, Reiss J, Lee Y-K et al (2011) Highly efficient capture of circulating tumor cells by using nanostructured silicon substrates with integrated chaotic micromixers. *Angew Chem Int Ed* 50(13):3084–3088
81. Zhao L, Lu Y-T, Li F, Wu K, Hou S, Yu J, Shen Q, Wu D, Song M, OuYang W-H et al (2013) High-purity prostate circulating tumor cell isolation by a polymer nanofiber-embedded microchip for whole exome sequencing. *Adv Mater* 25(21):2897–2902

82. Hou S, Zhao L, Shen Q, Yu J, Ng C, Kong X, Wu D, Song M, Shi X, Xu X et al (2013) Polymer nanofiber-embedded microchips for detection, isolation, and molecular analysis of single circulating melanoma cells. *Angew Chem Int Ed* 52(12):3379–3383
83. Shen Q, Xu L, Zhao L, Wu D, Fan Y, Zhou Y, OuYang W-H, Xu X, Zhang Z, Song M et al (2013) Specific capture and release of circulating tumor cells using aptamer-modified nanosubstrates. *Adv Mater* 25(16):2368–2373
84. Fröhlich E, Bonstingl G, Höfler A, Meindl C, Leitinger G, Pieber TR, Roblegg E (2013) Comparison of two in vitro systems to assess cellular effects of nanoparticles-containing aerosols. *Toxicol Vitro* 27(1):409–417
85. Adams DL, Zhu P, Makarova OV, Martin SS, Charpentier M, Chumsri S, Li S, Amstutz P, Tang C-M (2014) The systematic study of circulating tumor cell isolation using lithographic microfilters. *RSC Adv* 4(9):4334–4342
86. Czerlinski G, Reid D, Apostol A, Bauer K, Scarpelli D (1987) Determination of the density of cells from sedimentation studies at 1g. *J Biol Phys* 15(2):29–32
87. Dharmasiri U, Balamurugan S, Adams AA, Okagbare PI, Obubuafo A, Soper SA (2009) Highly efficient capture and enumeration of low abundance prostate cancer cells using prostate-specific membrane antigen aptamers immobilized to a polymeric microfluidic device. *Electrophoresis* 30(18):3289–3300
88. Staben ME, Zinchenko AZ, Davis RH (2003) Motion of a particle between two parallel plane walls in low-reynolds-number poiseuille flow. *Phys Fluids* 15(6):1711–1733
89. Cho YI, Kensey KR (1991) Effects of the non-newtonian viscosity of blood on flows in a diseased arterial vessel. part 1: steady flows. *Biorheology* 28(3–4):241–262